1 **Highly efficient p-i-n perovskite solar cells that endure temperature variations**

2 Guixiang Li,[1,10] Zhenhuang Su,[2,10] Laura Canil,[1] Declan Hughes,[3] Mahmoud H. Aldamasy,[1]
3 Janardan Dagar,[1] Sergei Trofimov,[1] Luyao Wang,[1]* Weiwei Zuo,[4] José J. Jerónimo-Rendon,[4]
4 Mahdi Malekshahi Byranvand,[4,5] Chenyue Wang,[2] Rui Zhu,[6] Zuhong Zhang,[6] Feng Yang,[6]
5 Giuseppe Nasti,[7] Boris Naydenov,[1] Wing C. Tsoi,[3] Zhe Li,[8] Xingyu Gao,[2] Zhaokui Wang,[9] Yu
6 Jia,[6] Eva Unger,[1] Michael Saliba,[4,5] Meng Li,[1,6,8]* and Antonio Abate[1,7]*

7 **Affiliations:**

8 [1] Helmholtz-Zentrum Berlin für Materialien und Energie GmbH, Hahn-Meitner-Platz 1, 14109
9 Berlin, Germany.

10 [2] Shanghai Synchrotron Radiation Facility (SSRF), Shanghai Advanced Research Institute,
11 Chinese Academy of Sciences, 239 Zhangheng Road, 201204 Shanghai, P. R. China.

12 [3] SPECIFIC, Department of Materials Science and Engineering, Faculty of Science and
13 Engineering, Swansea University, Bay Campus, Fabian Way, Swansea, SA1 8EN, UK.

14 [4] Institute for Photovoltaics (*ipv*), University of Stuttgart, Pfaffenwaldring 47, D-70569
15 Stuttgart, Germany.

16 [5] Helmholtz Young Investigator Group FRONTRUNNER, IEK5-Photovoltaics,
17 Forschungszentrum Jülich, 52425 Jülich, Germany.

18 [6] Key Lab for Special Functional Materials of Ministry of Education, National & Local Joint
19 Engineering Research Center for High-efficiency Display and Lighting Technology, School of
20 Materials Science and Engineering, Collaborative Innovation Center of Nano Functional
21 Materials and Applications, Henan University, Kaifeng 475004, China.

22 [7] Department of Chemical, Materials and Production Engineering, University of Naples
23 Federico II. Naples, pzz.le Vincenzo Tecchio 80, 80125 Naples, Italy.

24 [8] School of Engineering and Materials Science (SEMS), Queen Mary University of London,
25 London, E1 4NS, UK.

26 [9] Institute of Functional Nano & Soft Materials (FUNSOM), Jiangsu Key Laboratory for
27 Carbon-Based Functional Materials & Devices, Soochow University, 215123 Suzhou, China.

28 [10] These authors contributed equally.

29 *Corresponding author. Email: mengli@henu.edu.cn (M.L.); luyao.wang@helmholtz-
30 berlin.de (L.W.); antonio.abate@helmholtz-berlin.de (A.A.)

31

Abstract:

Daily temperature variations induce phase transitions and lattice strains in halide perovskites, challenging their stability in solar cells. We stabilised the perovskite black phase and improved the solar cell performance using the ordered dipolar structure of β-poly(1,1-difluoroethylene) to control the perovskite film crystallisation and the energy alignment. We demonstrated p-i-n perovskite solar cells with a record power conversion efficiency of 24.6% over 18 square millimetres and 23.1% over 1 square centimetre, which retained 96% and 88% of the efficiency after 1000-hours 1-sun maximum power point tracking at 25 and 75 °C, respectively. Devices under rapid thermal cycling between −60 °C and +80 °C showed no sign of fatigue, demonstrating the impact of the ordered dipolar structure on the operational stability of perovskite solar cells.

One-Sentence Summary:

Recorded 24.6% p-i-n perovskite solar cells achieve stable output against thermal cycling between −60 °C and +80 °C.

Main Text:

The highest power conversion efficiencies (PCEs) of >25% reported for single-junction perovskite solar cells (PSCs) rely on regular n-i-p architectures (*1*). However, inverted p-i-n PSCs have several advantages, including low-temperature processability and long-term operational stability derived from non-doped hole-transporting materials (*2, 3*). Nonetheless, they have lower PCEs, with only a few certified values exceeding 23% and a bottleneck value of 24% for over 10 square millimetre cells (*4–6*). This lower performance is mainly correlated with nonradiative recombination losses and reduced charge extraction that stem from the high density of defects in the perovskite bulk and interfacial contacts (*7, 8*).

For practical applications, ambient temperature variations can limit PSC performance (*9*) because the perovskite can undergo severe ion migration, phase transition, and temperature-induced strain, leading to lower PCE (*10–12*). Cycling over variable temperatures demands that the perovskite tolerate alternating tension and compression in the device structure (*13*). Thus, developing high-efficiency PSCs with thermal-cycle stability is critical to advancing the PSCs application.

Here, we utilise polymer dipoles to optimise triple-cation halide perovskite $Cs_{0.05}(FA_{0.98}MA_{0.02})_{0.95}Pb(I_{0.98}Br_{0.02})_3$ films from bulk to the surface. The polymer dipole promoted the growth of a low-defect crystalline film by reducing the formation energy of the black photoactive phase. The formation of dipoles at the perovskite surface suppressed ion migration and facilitated interfacial charge extraction while enhancing hydrophobicity. We achieved a certified PCE of 24.2% over an active area of 9.6 mm^2, and lab-recorded PCEs of 24.6% over 18 mm^2 and 23.1% over 1 cm^2. The high PCE was stable under severe thermal cycling from $-60\ °C$ to $+80\ °C$ for 120 cycles, demonstrating the resiliency of the crystal structure to the temperature-induced strains.

Film formation and characterisation

The alternate symmetric hydro and fluorocarbon units along the polymeric backbone of β-poly(1,1-difluoroethylene) (β-pV2F) result in an ordered molecular dipole distribution. 0.5 mg/mL β-pV2F of 180,000 molecular weight was used after screening a few molecular weights (**Figs. S1 and S2**). The influence of β-pV2F on the film morphology and work function is shown in **Fig. 1**. From the top-view and cross-sectional scanning electron microscope (SEM) images (**Fig. 1, A to C**), we can observe evident voids at the grain boundaries of the control perovskite film, with an average grain size of ~ 400 nm (**Fig. S3A**). These defects can create shunting paths and nonradiative recombination centres (*14*). β-pV2F enabled a more compact perovskite film with an enlarged grain size of around 480 nm (**Fig. 1, D to F**, and **Fig. S3B**). A smaller full-width at half-maximum in the (001) peak of the X-ray diffraction support an enhanced crystallinity in the β-pV2F-treated perovskite film (**Fig. S4**) (*15*). Furthermore, atomic force microscopy images showed that β-pV2F reduced the surface roughness from 54.4 nm to 41.1 nm (**Fig. S5**), which is expected to ameliorate coverage with charge-transporting layers (*16*).

Because of the electron-withdrawing effect of the fluorine atoms, the neighbouring hydrogen atoms have a partial positive charge density. Then, the all-trans planar zigzag (TTT) conformation of β-pV2F makes it resemble a Lewis acid, which can interact with the surface of the perovskite (*17, 18*). Fourier-transform infrared spectroscopy (FT-IR) revealed that the $–CH_2$ stretching vibration peak shifted from 3025 cm^{-1} of β-pV2F to 3019 cm^{-1} in contact with the target perovskite (**Fig. S6**), suggesting a solid C-H···X dipole interaction between $–CH_2$ moieties and halide ions of

[PbX$_6$]$^{4-}$ frame. Such polar interaction with the precursors of the perovskite influences the crystallisation during the film formation and leads to an upward shift of the surface work function (WF) after film formation (**Fig. 1G**) (*17*, *18*); **Fig. 1H** displays the increase in WF up to 300 meV for the target perovskite film, which facilitates the interfacial charge extraction and enhances the device's stability (*19*).

The WF shift was near that of standard perovskite film treated with *β*-pV2F only at the surface, which indicated that as the crystal growth proceeded, *β*-pV2F was partially expelled from the bulk and assembled on the perovskite surface (*2*, *20*). The fluorine-exposed surface arrangement induced hydrophobicity (**Figs. S7** and **S8**). We measured reduced nonradiative recombination and improved interfacial charge transfer in target perovskites (**Figs. S9-S13**) (*21–24*). This scenario is expected to enhance the solar cells' efficiency and stability (*25*, *26*).

To acquire an in-depth perspective on the promoted perovskite crystallisation kinetics, we performed synchrotron-based in situ grazing-incidence wide-angle x-ray scattering (GIWAXS) measurements to monitor the entire film formation process (several different stages are shown in **Fig. 2, A** and **B**). The initial t$_1$ stage (during the first 25 s) revealed the scattering halo at scattering vector q values from 8 to 8.5 nm^{-1} from the solvated colloidal sol precursor. The signal transition at t$_2$ (25 s) originated from dripping antisolvent, where the rapid solvent extraction caused the disappearance of the diffraction signal. Subsequently, the spin coating process was performed at stage t$_3$, where supersaturated solvate intermediate emerges. The t$_4$ near 60 s represented annealing stating. Stage t$_5$ revealed the intermediate phase signal with annealing. Stage t$_6$ was the perovskite evolution process. Stage t$_7$ described the cessation of further crystal growth.

Comparing GIWAXS patterns (**Fig. 2, A** and **B**), the weakened diffraction signal in the initial 60 s suggested the initial solvated phase of DMSO-DMF-PbX$_2$, where DMSO is dimethylsulfoxide, DMF is dimethylformamide, and X is a halide (I$^-$, Br$^-$), was suppressed. This effect could be ascribed to the initial solvated phase isolated by the long-chain *β*-pV2F molecules (*27*). The intermediate phase concentration was lower in the target than in the control (**Fig. S14**). The scattering feature centred at $q = \sim 10$ nm^{-1} along the (001) crystal plane observed in the cast film indicated that the colloid had solidified and converted into a black phase. Interestingly, we found that the perovskite phase of the target emerged earlier than that of the control ($\Delta t_t > \Delta t_c$), which implied that *β*-pV2F promoted the conversion of the intermediate phase to the perovskite black phase. The fast phase inversions were associated with the lower formation energy (*28*, *29*) and could be attributed to *β*-pV2F rapidly aggregating dispersed PbX$_2$ and organic salts during the elimination of DMSO and DMF (*30*).

Moreover, the target ceased crystal growth sooner at 250 s than the control at 350 s. When the crystallisation is completed (stage t$_7$), the signal is more intense in the target than in the control (**Fig. 2C**). This result indicates that the target perovskite film is more ordered. The time-dependent in situ GIWAXS intensity profiles with other scattering vectors, such as $q = \sim 20$ nm^{-1} corresponding to the (002) crystal plane (**Fig. S15**), showed the same phase transition trend. Thus, *β*-pV2F control the perovskite crystallisation kinetics by lowering the perovskite formation energy, promoting phase conversion, and enabling a more ordered crystal structure (**Fig. S16**).

Photovoltaic performance

The photovoltaic performance of inverted p-i-n PSCs with control and polymer-modified perovskite films is shown in **Fig. 3**. The device architecture is glass/ indium tin oxide (ITO)/ self-

1   assembled   [2-(3,6-dimethoxy-9H-carbazol-9-yl)ethyl]phosphonic   acid   (MeO-2PACz)/
2   perovskite/ [6,6]-phenyl-C61-butyric acid methyl ester ($PC_{61}BM$)/ bathocuproine (BCP)/ silver
3   (Ag) (**Fig. S17**). Typical current-voltage (*J-V*) curves for the PSCs (**Fig. 3A**) were measured with
4   a device area of 18 mm^2. The control PSCs had a PCE of 22.3%, with short-circuit current density
5   (J_{sc}) of 24.7 mA/cm^2, V_{oc} of 1.13 V, and fill factor (FF) of 80.2%. With β-pV2F, the device
6   performance improved with a V_{oc} of 1.18 V, J_{sc} of 24.8 mA/cm^2, and FF of 84.3% for a PCE of
7   24.6%. Target PSCs' reverse- and forward-sweep J-V curves (Fig. S18) had negligible hysteresis.
8   A PCE of 24.2% for an aperture area of 9.6 mm^2 is obtained from an independent accredited
9   certification institute of Test and Calibration Center of New Energy Device and Module, Shanghai
10   Institute of Microsystem and Information Technology (SIMIT), Chinese Academy of Sciences
11   (**Fig. S19**). We also recorded a PCE of 23.1% for devices with a working area of 1 cm^2 (**Fig. 3B**).

12   From the external quantum efficiency (EQE) spectra (**Fig. 3C**), we calculated an integrated J_{sc} of
13   24.3 and 24.4 mA/cm^2 for control and target devices, respectively, comparable to the values
14   extracted from the *J-V* curves. The optical bandgaps of both perovskite absorbers determined by
15   the x-axis intercept of the EQE linear are shown in **Fig. S20** (*31, 32*). The statistical distribution
16   of the device parameters collected from 38 devices shows an improved PV performance and
17   increased reproducibility with β-pV2F (**Fig. S21**) (*33*), which we explain with a better charge
18   extraction and reduced nonradiative recombination (*27*).

19   The stabilised power outputs at the maximum power point (MPP) are plotted in **Fig. 3D**. The
20   control device showed a persistent attenuation in efficiency under continuous 1 equivalent sun
21   illumination for 400 s. In contrast, the tracked target device yielded highly stable power output and
22   even progressively improved performance, which we attributed to the light-soaking effect (*34*).
23   Unencapsulated devices' stability under working conditions shows that target PSCs retain 96% of
24   the initial PCE after continuous MPP tracking for 1000 h. In contrast, control PSCs decay to 84%
25   of their original PCE (**Fig. 3E**). Device stability statistics (*n* = 12) were presented in **Fig. S22**.
26   Heating the device to 75 °C, 88% PCE was retained in the target device and only 56% in the control
27   (**Fig. S23**).

28   We further evaluated device stability against temperature variations. The *J-V* curves in **Fig. S24**
29   show that the control device's PV parameters (J_{sc}, FF and V_{oc}) exhibited large fluctuations when
30   tested at temperatures ranging from −60 to +80 °C (**Table S1**). However, this variation was
31   suppressed in the target device (**Fig. S25** and **Table S2**). Furthermore, compared to the control,
32   the target device had reduced hysteresis, and its hysteresis factor is relatively stable under
33   temperature variations (**Fig. S26**). The statistical PCE distribution in **Fig. 4 A** and **B** indicates that
34   the β-pV2F stabilisation effect is highly reproducible. All performance parameter evolution is
35   reported in **Figs. S27** and **S28**. Subsequently, the unencapsulated devices were aged under rapid
36   thermal cycling (TC) between −60 °C and +80 °C, swept at a 20 °C/min rate. As shown in **Fig. 4,**
37   **C** and **D**, the control device suffered a severe decline of 75.6% at +80 °C and 63.0% at −60 °C,
38   whereas the target device retained 93.9% at 80 °C and 88.7% at −60 °C of its initial value after
39   120 thermal cycles.

40

41   **Device film morphologies and structures during thermal cycling**

42   The difference in device performance stems from using β-pV2F in the perovskite film. We
43   characterised the morphology and crystal structure of perovskite films undergoing ageing with
44   thermal cycling to identify the impact of β-pV2F. The film ageing followed the same device
45   protocol: 120 rapid thermal cycling between −60 °C and +80 °C at a 20 °C/min rate. As observed

from the SEM images in **Fig. S29**, control films exhibited severe morphological degradation with enlarged grain boundaries and voids. Such degradation features were not detected in the aged target films (**Fig. S30**), which appeared nearly identical to the pristine film shown in **Fig. 1E**. This result indicates that the temperature-induced degradation of perovskite films is suppressed in target perovskites (**Fig. S31**) (*35*).

We observed additional GIWAXS peaks forming in the control perovskite after three thermal cycles (**Fig. 5A**). Specifically, in the second cycle, the peak for PbI_2, a degradation product, emerged at $q = 9.2$ nm^{-1}. During the third thermal cycle, additional peaks around 8.2 and 8.6 nm^{-1} formed, corresponding to the hexagonal photoinactive polytypes 4H and 6H from $Cs_{0.05}(FA_{0.98}MA_{0.02})_{0.95}Pb(I_{0.98}Br_{0.02})_3$ perovskite (**Fig. S32A**) (*36*, *37*). This result indicates that the control perovskite undergoes irreversible phase changes. The generation of these phases may originate from the lattice deformation at the grain boundaries caused by the mutual extrusion of unit cells from neighbored crystals of different orientations (*36*). Such phenomena were not observed in the target perovskite (**Fig. 5B**), indicating high structural stability (**Fig. S32B**).

For q values from 16 to 19 nm^{-1}, we observed additional peaks in both control and target (**Figs. S33** and **S34**), corresponding to the tetragonal phase (β phase) (*10*, *38*). The tetragonal phase was only retained in the cold temperature region. This suggests that the degradation products of perovskite under thermal cycling include irreversible PbI_2, 4H and 6H, and reversible tetragonal phase transition, jointly contributing to the device performance degradation. Temperature-resolved azimuthally-integrated intensity patterns (**Figs. S35** and **S36**) indicate that β-pV2 suppress the phase transitions. We found that suppressing the phase transition also suppressed the ion migration in the complete device under working conditions, i.e., lower hysteresis (**Fig. S37**).

Due to differences in thermal expansion coefficients between the perovskite film and the substrate, temperature variation induces strain in the perovskite (*39*, *40*). The control perovskite underwent substantial lattice strain evolution (−0.13% to 0.57%) during thermal cycling (**Fig. 5C**). We observed that the perovskite strain drifted with temperature cycling, showing a constant lattice parameter change in perovskite. In contrast, the target perovskite exhibits stable strain cycling in a narrower range (−0.06% to 0.38%), corresponding to a recoverable crystal structure and releasable lattice strain (**Tables S3-S5**). We propose that a strain-buffering and lattice-stabilizing effect exists in target perovskite because β-pV2F creates a self-assembly polymeric layer that coats the crystals within the perovskite film reducing friction during thermal cycling (**Figs. S38** and **S39**) (*41*–*44*).

Conclusions

Thermal stress experienced in normal working conditions induces phase transitions and lattice strains that hamper the stability of perovskite solar cells (PSCs). Coating the crystals comprising the perovskite film with polymer dipoles results in a strain-buffering and lattice-stabilizing effect that mitigates the impact of thermal stress. We selected the specific polymer dipole β-poly(1,1-difluoroethylene) (β-pV2F). The β-pV2F highly ordered dipolar structure interacts with specific perovskite components enabling control of the perovskite film crystallisation during the processing and energy alignment with the charge-selective contacts within the device. We reported β-pV2F devices with improved power conversion efficiency up to 24.6% on an active area of 18 mm^2 and 23.1% over a larger area of 1 cm^2 (certified PCE of 24.24% with an active area of 9.6 mm^2 from SIMIT). The β-pV2F strain-buffering effects enabled stable power output at temperatures as high

as 75 °C and rapid temperature variation between −60 °C and +80 °C. Our work identifies a new strategy to make stable perovskite solar cells.

References and Notes

1. *Best Research-Cell Efficiencies*, https://www.nrel.gov/pv/assets/pdfs/best-research-cell-efficiencies-rev220126.pdf

2. X. Zheng *et al.*, Managing grains and interfaces via ligand anchoring enables 22.3%-efficiency inverted perovskite solar cells. *Nat. Energy* **5**, 131-140 (2020).

3. Y.-N. Lu *et al.*, Constructing an n/n$^+$ homojunction in a monolithic perovskite film for boosting charge collection in inverted perovskite photovoltaics. *Energy Environ. Sci.* **14**, 4048-4058 (2021).

4. Z. Li *et al.*, Organometallic-functionalized interfaces for highly efficient inverted perovskite solar cells. *Science* **376**, 416-420 (2022).

5. H. Chen *et al.*, Quantum-size-tuned heterostructures enable efficient and stable inverted perovskite solar cells. *Nat. Photonics* **16**, 352-358 (2022).

6. X. Li *et al.*, Constructing heterojunctions by surface sulfidation for efficient inverted perovskite solar cells. *Science* **375**, 434-437 (2022).

7. M. Degani *et al.*, 23.7% Efficient inverted perovskite solar cells by dual interfacial modification. *Sci. Adv.* **7**, eabj7930 (2021).

8. D. Luo *et al.*, Enhanced photovoltage for inverted planar heterojunction perovskite solar cells. *Science* **360**, 1442-1446 (2018).

9. W. Tress *et al.*, Performance of perovskite solar cells under simulated temperature-illumination real-world operating conditions. *Nat. Energy* **4**, 568-574 (2019).

10. S. Kahmann *et al.*, Compositional variation in FAPb$_{1-x}$Sn$_x$I$_3$ and its impact on the electronic structure: a combined density functional theory and experimental study. *ACS Appl. Mater. Interfaces* (2022).

11. X. Zhang, S.-H. Wei, Origin of efficiency enhancement by lattice expansion in hybrid-perovskite solar cells. *Phys. Rev. Lett.* **128**, 136401 (2022).

12. D.-J. Xue *et al.*, Regulating strain in perovskite thin films through charge-transport layers. *Nat. Commun.* **11**, 1514 (2020).

13. R. Cheacharoen *et al.*, Design and understanding of encapsulated perovskite solar cells to withstand temperature cycling. *Energy Environ. Sci.* **11**, 144-150 (2018).

14. C. Sun *et al.*, High-performance large-area quasi-2D perovskite light-emitting diodes. *Nat. Commun.* **12**, 2207 (2021).

15. Z. Wang *et al.*, Efficient ambient-air-stable solar cells with 2D–3D heterostructured butylammonium-caesium-formamidinium lead halide perovskites. *Nat. Energy* **2**, 17135 (2017).

16. L. Xu *et al.*, Resonance-mediated dynamic modulation of perovskite crystallisation for efficient and stable solar cells. *Adv. Mater.* **34**, 2107111 (2022).

17. L. Canil *et al.*, Tuning halide perovskite energy levels. *Energy Environ. Sci.* **14**, 1429-1438 (2021).

18. A. J. de Jesus Silva, M. M. Contreras, C. R. Nascimento, M. F. da Costa, Kinetics of thermal degradation and lifetime study of poly(vinylidene fluoride) (PVDF) subjected to bioethanol fuel accelerated ageing. *Heliyon* **6**, e04573 (2020).

19. P. Metrangolo, L. Canil, A. Abate, G. Terraneo, G. Cavallo, Halogen bonding in perovskite solar cells: a new tool for improving solar energy conversion. *Angew. Chem. Int. Ed.* **61**, e202114793 (2022).

20. Y. Moriya, R. Ishikawa, S. Akiyama, K. Ueno, H. Shirai, Self-assembled fluorinated polymer passivation layer for efficient perovskite thin-film solar cells. *Chem. Lett.* **49**, 87-90 (2019).

21. J. Jeong *et al.*, Pseudo-halide anion engineering for α-FAPbI$_3$ perovskite solar cells. *Nature* **592**, 381-385 (2021).

22. G. Li *et al.*, Ionic liquid stabilizing high-efficiency tin halide perovskite solar cells. *Adv. Energy Mater.* **11**, 2101539 (2021).

23. D. Koo *et al.*, High-performance inverted perovskite solar cells with operational stability via n-type small molecule additive-assisted defect passivation. *Adv. Energy Mater.* **10**, 2001920 (2020).

24. S. Chen *et al.*, Stabilizing perovskite-substrate interfaces for high-performance perovskite modules. *Science* **373**, 902-907 (2021).

25. M. Stolterfoht *et al.*, How to quantify the efficiency potential of neat perovskite films: perovskite semiconductors with an implied efficiency exceeding 28%. *Adv. Mater.* **32**, 2000080 (2020).

26. L. Canil *et al.*, Halogen-bonded hole-transport material suppresses charge recombination and enhances stability of perovskite solar cells. *Adv. Energy Mater.* **11**, 2101553 (2021).

27. Y. Li *et al.*, Efficient, stable formamidinium-cesium perovskite solar cells and minimodules enabled by crystallization regulation. *Joule* **6**, 676-689 (2022).

28. Y. Cho *et al.*, Mixed 3D–2D passivation treatment for mixed-cation lead mixed-halide perovskite solar cells for higher efficiency and better stability. *Adv. Energy Mater.* **8**, 1703392 (2018).

29. H. Hu *et al.*, Nucleation and crystal growth control for scalable solution-processed organic–inorganic hybrid perovskite solar cells. *J. Mater. Chem. A* **8**, 1578-1603 (2020).

30. M. Qin *et al.*, Precise Control of Perovskite Crystallization Kinetics via Sequential A-Site Doping. *Adv. Mater.* **32**, 2004630 (2020).

31. A. Y. Alsalloum *et al.*, 22.8%-Efficient single-crystal mixed-cation inverted perovskite solar cells with a near-optimal bandgap. *Energy Environ. Sci.* **14**, 2263-2268 (2021).

32. P. S. C. Schulze *et al.*, 25.1% High-efficiency monolithic perovskite silicon tandem solar cell with a high bandgap perovskite absorber. *Sol. RRL* **4**, 2000152 (2020).

33. R. Azmi *et al.*, Damp heat–stable perovskite solar cells with tailored-dimensionality 2D/3D heterojunctions. *Science* **376**, 73-77 (2022).

34. S. Wu *et al.*, Modulation of defects and interfaces through alkylammonium interlayer for efficient inverted perovskite solar cells. *Joule* **4**, 1248-1262 (2020).

35. Z. Dai *et al.*, Interfacial toughening with self-assembled monolayers enhances perovskite solar cell reliability. *Science* **372**, 618-622 (2021).

36. M. Qin *et al.*, Manipulating the mixed-perovskite crystallization pathway unveiled by in situ GIWAXS. *Adv. Mater.* **31**, 1901284 (2019).

37. P. Gratia *et al.*, The many faces of mixed ion perovskites: unraveling and understanding the crystallization process. *ACS Energy Lett.* **2**, 2686-2693 (2017).

38. W. Peng *et al.*, Engineering of $CH_3NH_3PbI_3$ perovskite crystals by alloying large organic cations for enhanced thermal stability and transport properties. *Angew. Chem. Int. Ed.* **55**, 10686-10690 (2016).

39. C. Zhu *et al.*, Strain engineering in perovskite solar cells and its impacts on carrier dynamics. *Nat. Commun.* **10**, 815 (2019).

40. J. Zhao *et al.*, Strained hybrid perovskite thin films and their impact on the intrinsic stability of perovskite solar cells. *Sci. Adv.* **3**, eaao5616 (2017).

41. L. Wang, Q. Gong, S. Zhan, L. Jiang, Y. Zheng, Robust anti-icing performance of a flexible superhydrophobic surface. *Adv. Mater.* **28**, 7729-7735 (2016).

42. L. T. Hieu, S. So, I. T. Kim, J. Hur, Zn anode with flexible β-PVDF coating for aqueous Zn-ion batteries with long cycle life. *Chem. Eng. J.* **411**, 128584 (2021).

43. W. Chen *et al.*, Conjugated polymer–assisted grain boundary passivation for efficient inverted planar perovskite solar cells. *Adv. Funct. Mater.* **29**, 1808855 (2019).

44. L. Zuo *et al.*, Polymer-modified halide perovskite films for efficient and stable planar heterojunction solar cells. *Sci. adv.* **3**, e1700106 (2017).

45. S. N. Habisreutinger, N. K. Noel, H. J. Snaith, Hysteresis Index: A Figure without Merit for Quantifying Hysteresis in Perovskite Solar Cells. *ACS Energy Lett.* **3**, 2472-2476 (2018).

46. H. Wang *et al.*, Interfacial Residual Stress Relaxation in Perovskite Solar Cells with Improved Stability. *Adv. Mater.* **31**, 1904408 (2019).

47. N. Rolston *et al.*, Engineering Stress in Perovskite Solar Cells to Improve Stability. *Adv. Energy Mater.* **8**, 1802139 (2018).

48. M. A. Reyes-Martinez *et al.*, Time-Dependent Mechanical Response of $APbX_3$ (A = Cs, CH_3NH_3; X = I, Br) Single Crystals. *Adv. Mater.* **29**, 1606556 (2017).

49. J. Yu, M. Wang, S. Lin, Probing the Soft and Nanoductile Mechanical Nature of Single and Polycrystalline Organic–Inorganic Hybrid Perovskites for Flexible Functional Devices. *ACS Nano* **10**, 11044-11057 (2016).

50. S. K. Karan *et al.*, Designing high energy conversion efficient bio-inspired vitamin assisted single-structured based self-powered piezoelectric/wind/acoustic multi-energy harvester with remarkable power density. *Nano Energy* **59**, 169-183 (2019).

51. A. Tamang *et al.*, DNA-Assisted β-phase Nucleation and Alignment of Molecular Dipoles in PVDF Film: A Realization of Self-Poled Bioinspired Flexible Polymer Nanogenerator for Portable Electronic Devices. *ACS Appl. Mater. Interfaces* **7**, 16143-16147 (2015).

52. M. Wang *et al.*, Small Molecule Modulator at the Interface for Efficient Perovskite Solar Cells with High Short-Circuit Current Density and Hysteresis Free. *Adv. Electron. Mater.* **6**, 2000604 (2020).

1 under the European Union's Horizon 2020 research and innovation programme (grant
2 agreement 804519).

3 **Author contributions:** G.L., L.W., M.L. and A.A. conceived the idea. G.L. and M.L. designed
4 the experiments. G.L., Z.S., L.W., S.T., M.H.M., Z.Z, F.Y. and M.L. fabricated and
5 characterised perovskite films and devices. Z.S. and C.W. conducted the GIWAXS
6 measurements. G.L., D.H., L.W., W.Z., R.Z., F.Y., Y.J., and M.L. performed the device
7 performance measurements. G.L., Z.S., L.C., L.W., M.L. and A.A. participated in the data
8 analysis and result discussions. G.L. composed the manuscript. D.H., M.H.M., J.D., S.T.,
9 W.Z., J.J.J.-R., M.M.B., G.N., B.N., M.L. and A.A. contributed to suggestions for the
10 manuscript. L.W., W.C.T., Z.L., X.G., Z.W., E.U., M.S., M.L. and A.A. provided expertise
11 and supervised the work. All authors reviewed the manuscript.

12 **Competing interests:** Authors declare that they have no competing interests.

13 **Data and materials availability:** All data are available in the manuscript or the supplementary
14 materials.

15 **Supplementary Materials**

16 Materials and Methods

17 Supplementary Text

18 Figs. S1 to S39

19 Tables S1 to S5

20 References (*45–52*)

21
22
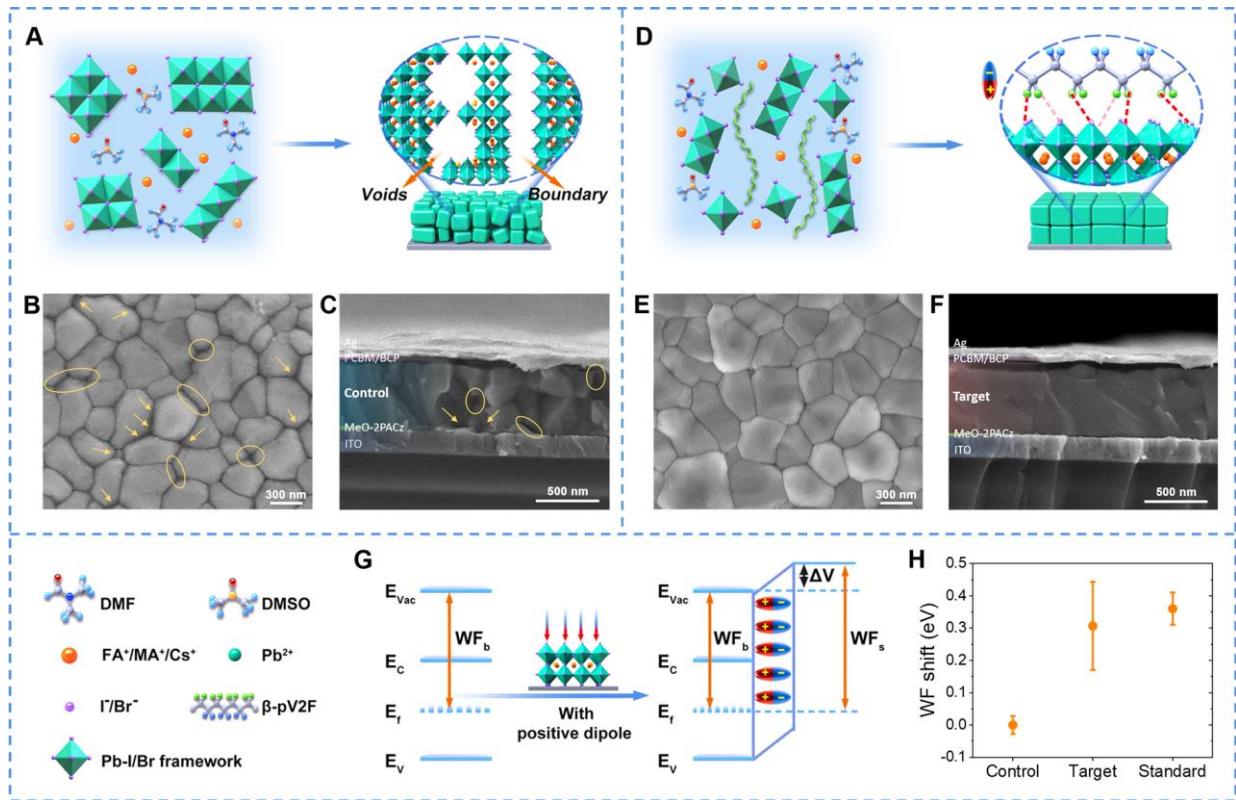
Fig. 1. Working mechanism and morphology characterisation of perovskite films. Schematic of processing (**A**) control and (**D**) target perovskites. (**B**) Top-view and (**C**) cross-sectional SEM images of control perovskites. (**E**) Top-view and (**F**) cross-sectional SEM images of target perovskites. (**G**, **H**) WF shift related to perovskite functionalised with β-pV2F.

1

2
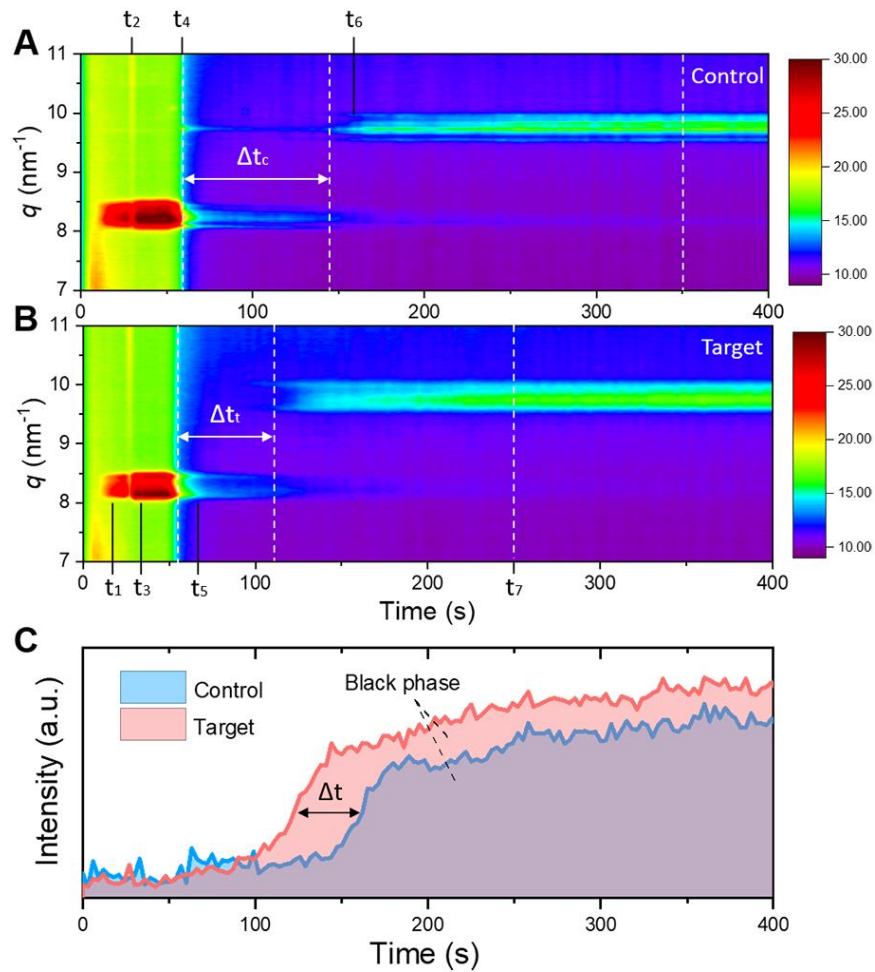
Fig. 2. Crystallization kinetics of perovskite films. In situ GIWAXS spectra during forming (**A**) control and (**B**) target perovskite films. (**C**) Time-resolved integrated peak area intensity for black phases of control and target perovskites.

1

2
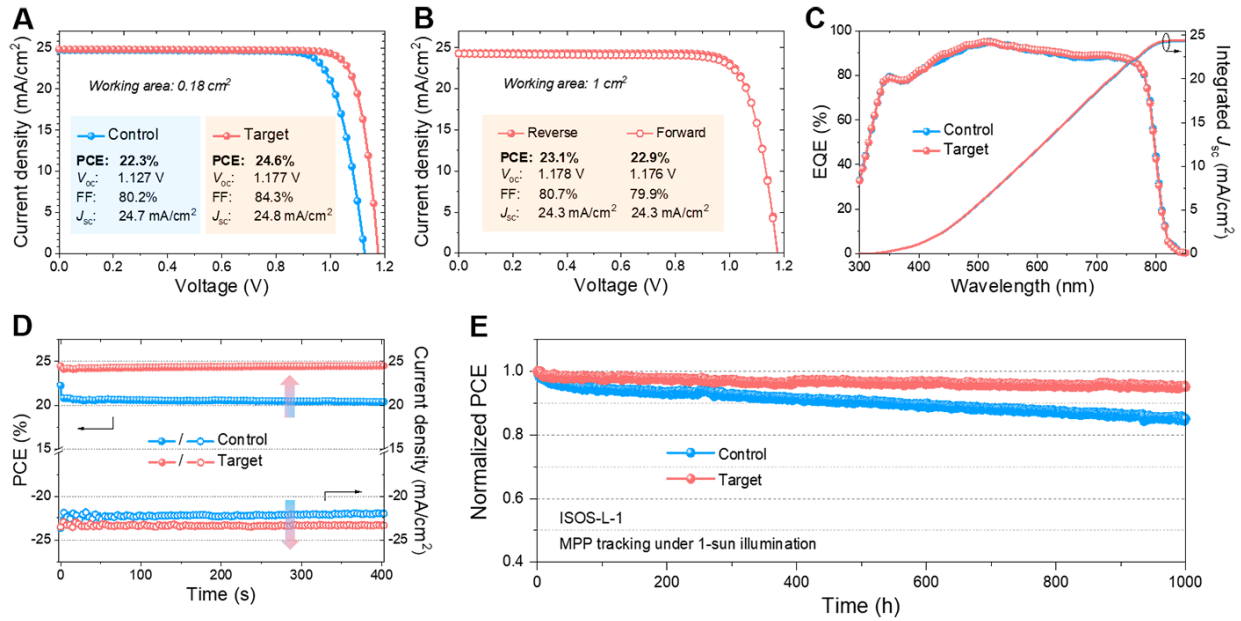
Fig. 3. PV performance of perovskite solar cells. (**A**) *J-V* curves of control and target PSCs under a device area of 0.18 cm^2. (**B**) *J-V* curves with the reverse and forward sweep for large-area target PSCs (1 cm^2). (**C**) EQE spectra and integrated J_{sc} for control and target PSCs. (**D**) Stabilised power outputs with evolving current density at the maximum power points as a function of time for the best-performing PSCs. (**E**) Long-term stability at maximum power point tracking under room-temperature continuous illumination in N$_2$ atmosphere for unencapsulated PSCs (ISOS-L-1 procedure).

1
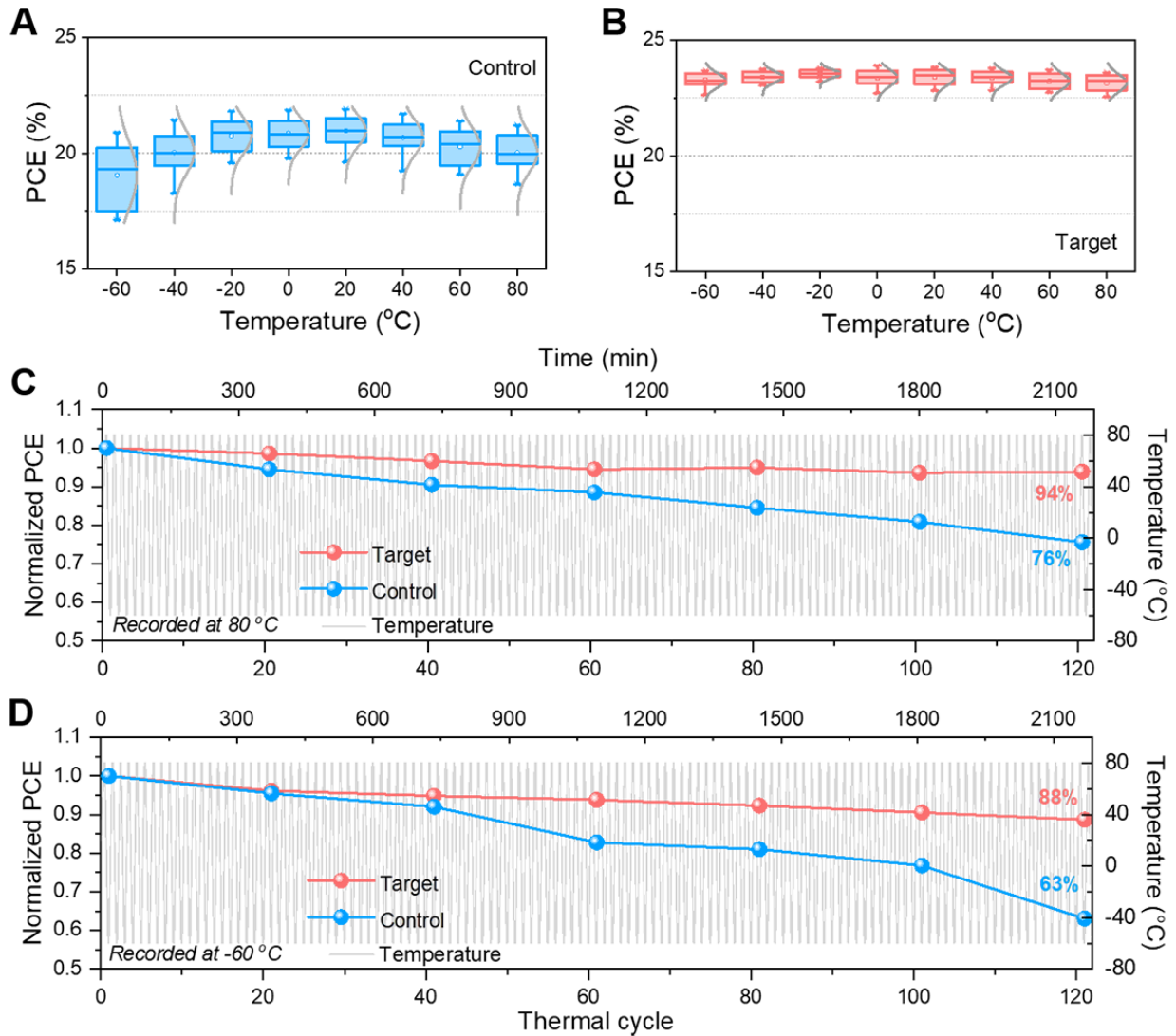
Fig. 4. Thermal cycling stability of perovskite solar cells. Statistical temperature-dependence PCE profiles of (**A**) control PSCs and (**B**) target PSCs. PCE evolution recorded at (**C**) +80 °C (**D**) −60 °C of control and target PSCs against thermal cycles between −60 °C and +80 °C. (The rapid thermal cycling was implemented with a 20 °C/min ramp rate. There is an extra 2-minute waiting window for the device to reach thermal equilibrium when cycling to −60 °C and +80 °C. The temperature starts from room temperature, heating to +80 °C and then cooling to −60 °C. The progress ends at room temperature. The time per complete cycle is 18 min.)

1
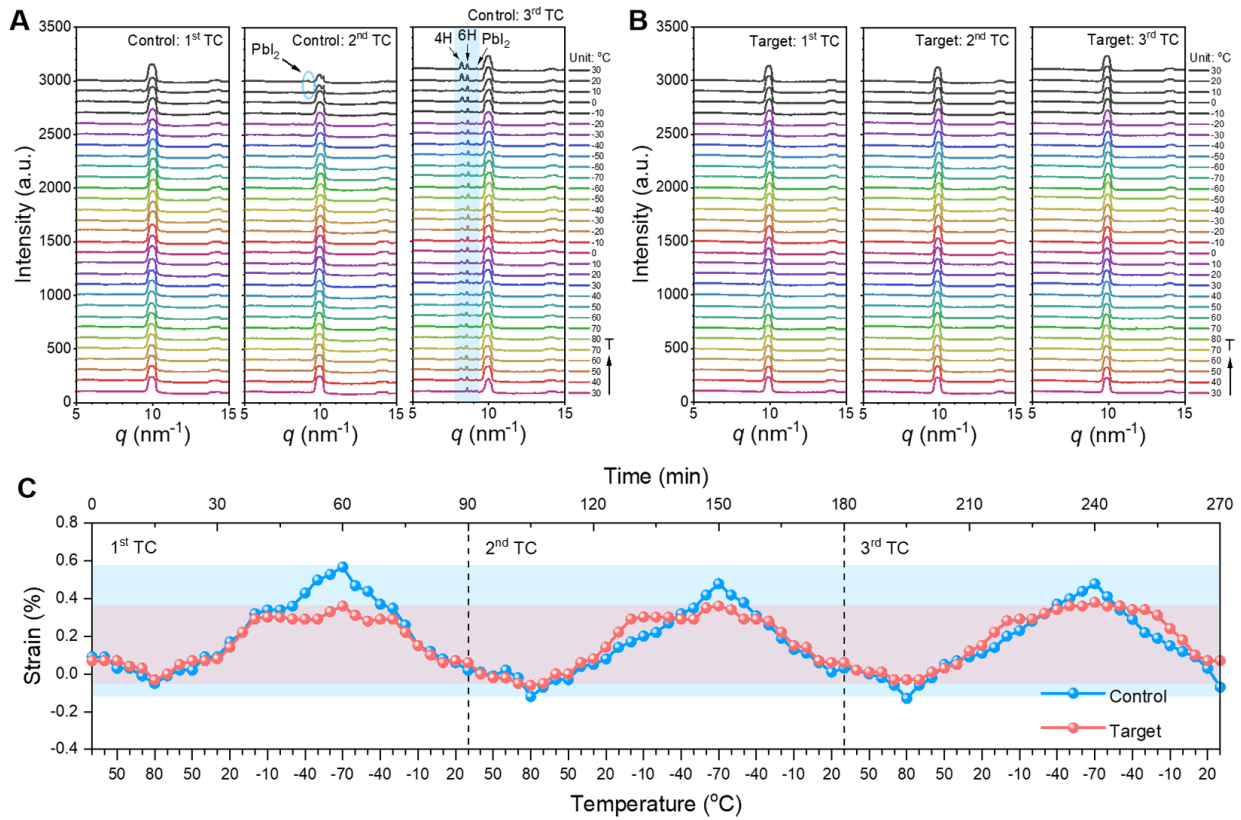
Fig. 5. Perovskite structural evolution during temperature cycling. The temperature-resolved GIWAXS profiles for (**A**) control and (**B**) target perovskites. (**C**) The temperature-resolved lattice strain for control and target perovskites. (The temperature starts from room temperature, heating to +80 °C and then cooling to −60 °C. The progress ends at room temperature. The time per complete cycle is 90 min.)